



Publication Year	2017
Acceptance in OA @INAF	2022-07-15T15:35:41Z
Title	A High-Resolution Radio Continuum Study Of The Dwarf Irregular Galaxy IC 10
Authors	Westcott, J.; Brinks, E.; Beswick, R. J.; Heesen, V.; Argo, M. K.; et al.
DOI	10.1093/mnras/stx188
Handle	http://hdl.handle.net/20.500.12386/32511
Journal	MONTHLY NOTICES OF THE ROYAL ASTRONOMICAL SOCIETY
Number	467

A high-resolution radio continuum study of the dwarf irregular galaxy IC 10

J. Westcott,^{1★} E. Brinks,¹ R. J. Beswick,² V. Heesen,^{3,4} M. K. Argo,^{2,5} R. D. Baldi,⁴
D. M. Fenech,⁶ I. M. McHardy,⁴ D. J. B. Smith¹ and D. R. A. Williams⁴

¹Centre for Astrophysics Research, University of Hertfordshire, College Lane, Hatfield, AL10 9AB, UK

²Jodrell Bank Centre for Astrophysics, School of Physics and Astronomy, The University of Manchester, Manchester M13 9PL, UK

³Hamburger Sternwarte, Universität Hamburg, Gojenbergsweg 112, D-21029 Hamburg, Germany

⁴School of Physics and Astronomy, University of Southampton, Southampton SO17 1BJ, UK

⁵Jeremiah Horrocks Institute, University of Central Lancashire, Preston PR1 2HE, UK

⁶Department of Physics and Astronomy, University College London, Gower Street, London, WC1E 6BT, UK

Accepted 2017 January 19. Received 2017 January 17; in original form 2016 October 17

ABSTRACT

We present high-resolution e-Multi-Element Radio Linked Interferometer Network radio continuum maps of the dwarf irregular galaxy IC 10 at 1.5 and 5 GHz. We detect 11 compact sources at 1.5 GHz, five of which have complementary detections at 5 GHz. We classify three extended sources as compact H II regions within IC 10, five sources as contaminating background galaxies and identify three sources that require additional observations to classify. We do not expect that any of these three sources are supernova remnants as they will likely be resolved out at the assumed distance of IC 10 (0.7 Mpc). We correct integrated flux densities of IC 10 from the literature for contamination by unrelated background sources and obtain updated flux density measurements of 354 ± 11 mJy at 1.5 GHz and 199 ± 9 mJy at 4.85 GHz. The background contamination does not contribute significantly to the overall radio emission from IC 10, so previous analysis concerning its integrated radio properties remains valid.

Key words: techniques: high angular resolution – techniques: interferometric – H II regions – ISM: supernova remnants – galaxies: dwarf – galaxies: ISM.

1 INTRODUCTION

Radio emission within normal galaxies originates from the evolution and death of massive stars ($\geq 8 M_{\odot}$), and hence effectively traces recent star formation (SF; Condon 1992). Since it is not subject to extinction by dust, radio emission should be an ideal tracer of SF that would be valid out to the highest redshifts. At the time of writing, radio luminosity is calibrated as a star formation rate (SFR) indicator via the radio–FIR relation (Bell 2003), a tight correlation that links both FIR and radio emission to massive SF. Yet the physical origin of this correlation is not fully understood, with many seemingly independent factors balancing out to form a ‘cosmic conspiracy’ (Condon 1992; Appleton et al. 2004; Lacki, Thompson & Quataert 2010). This then makes it desirable to calibrate the radio–SF relation without recourse to the FIR data.

The Legacy e-MERLIN Multi-band Imaging of Nearby Galaxies (LeMMINGs; Beswick et al. 2014) survey aims, in part, to address this by studying compact SF products and their relation to large-scale radio emission across a wide range of galaxy type. The

project is made up of two complementary surveys of nearby galaxies: a statistical survey of 280 galaxies taken in snapshot mode, comprising the entire Palomar spectroscopic bright galaxy sample north of declination +20 deg, and a deep survey of six galaxies, the latter reaching rms sensitivities of 8 and 3 $\mu\text{Jy beam}^{-1}$ at 1.5 and 5 GHz, respectively. The statistical survey will detect and resolve radio emission from supernovae (SNe) and supernova remnants (SNR) to provide a complete census of energetic SF products in the local Universe. At higher sensitivities, the deep survey will also be able to detect faint radio emission from planetary nebulae, H II regions and superstar clusters. Together, these surveys will be used to calibrate the SFR in nearby galaxies on the basis of compact radio source populations, independent of obscuration by dust. The nearby dwarf irregular galaxy IC 10 (see Fig. 1) was observed during the commissioning phase of the upgraded e-MERLIN array and is the first galaxy to be observed as part of the LeMMINGs deep survey.

IC 10 is thought to be currently undergoing a starburst phase (Leroy et al. 2006), with optical studies revealing numerous H II regions (Hodge & Lee 1990) and the highest density of Wolf-Rayet (WR) stars observed in the Local Group (Massey, Armandroff & Conti 1992; Crowther et al. 2003). Moreover, stellar population analysis reveals a bursty SF history with the most recent burst

* E-mail: j.westcott3@herts.ac.uk

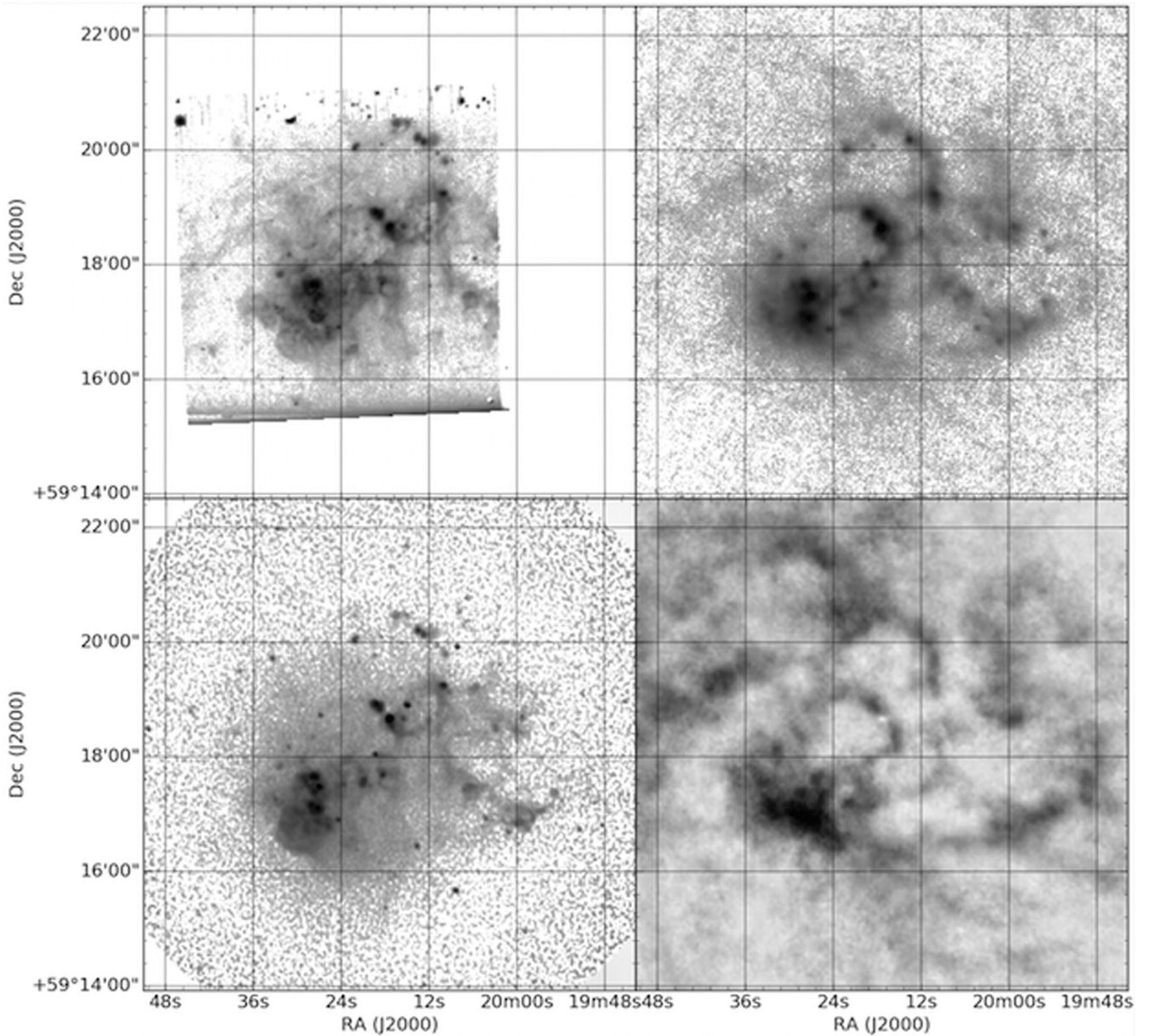


Figure 1. IC 10 at multiple wavelengths. Top left: $H\alpha$ continuum subtracted map taken from Hunter & Elmegreen (2004). Top right: map of IC 10 at 70 μm taken with *Herschel* as part of the Dwarf Galaxy Survey (Madden et al. 2013). Bottom left: 5-GHz VLA C and D array map of IC 10 taken from Heesen et al. (2015). Bottom right: naturally weighted $H\text{I}$ map of IC 10 taken as part of LITTLE THINGS (Hunter et al. 2012). Note how the large-scale holes and shells in the $H\text{I}$ distribution can be easily identified across multiple wavelengths.

finishing ~ 10 Myr ago (Hunter 2001; Vacca, Sheehy & Graham 2007; Sanna et al. 2009). A brief summary of the properties of IC 10 is presented in Table 1.

Recent radio investigations into the large-scale gas motions of IC 10 reveal a complex nature, consisting of a large $H\text{I}$ envelope with an inner rotating disc and counter-rotating component (Shostak & Skillman 1989; Wilcots & Miller 1998; Ashley et al. 2014). The leading explanation for these different kinematical subsystems is that IC 10 is still accreting primordial gas (Wilcots & Miller 1998), although new evidence hints towards a recent merger or interaction being responsible for the unusual gas kinematics and current starburst (Nidever et al. 2013; Ashley et al. 2014). Furthermore, numerous bubbles and shells are observed in the large-scale $H\text{I}$

Table 1. Key IC 10 properties.

Property	Value	Reference
α_{J2000}	00 20 17.34	–
δ_{J2000}	+59 18 13.6	–
Galaxy type	IBm	1
Distance	0.7 Mpc	2
$\text{SFR}_{H\alpha}$	$0.039 \pm 0.001 M_{\odot} \text{ yr}^{-1}$	3
Angular size (major axis)	11'68	4
Angular size (minor axis)	7'12	4
Position angle	132°	4

Reference list: (1) Nilson (1973), (2) Sakai, Madore & Freedman (1999), (3) Hunter et al. (2012), (4) Jarrett et al. (2003).

Table 2. Journal of IC 10 e-MERLIN observations.

Obs. date (yyyy mmm dd)	Obs. frequency (MHz)	Total bandwidth (MHz)	Time (h)
2013 Feb 09	1510.65	512	7.64
2013 Nov 22	1526.65	512	16.24
2015 Apr 18	5072.50	512	21.06
2016 Feb 21	5072.50	512	9.24

Notes. Obs. frequency is the central observed frequency and time is the total time on source.

distribution (Shostak & Skillman 1989; Wilcots & Miller 1998), hinting that IC 10 is coming towards the end of its current starburst phase (see the bottom-right panel in Fig. 1). A number of radio continuum studies focused on the non-thermal superbubble (NTSB) towards the south-east of IC 10 (Yang & Skillman 1993; Heesen et al. 2015), which is thought to be the result of either a collection of SNR (Yang & Skillman 1993) or a single hypernova event (Lozinskaya & Moiseev 2007). At its centre resides the X-ray binary system, IC 10 X-1, which is likely related to the birth and evolution of the superbubble (Brandt et al. 1997; Bauer & Brandt 2004).

IC 10 is located at a low galactic latitude ($\sim -3^\circ$), making distance measurements challenging with estimates ranging from 0.5 to 3 Mpc (Demers, Battinelli & Letarte 2004; Kim et al. 2009). In this paper, we will assume a distance to IC 10 of 0.7 Mpc (1 arcsec $\simeq 3.4$ pc), as listed in Hunter et al. (2012); we scale all literature measurements used here to this distance.

The paper is structured as follows: in Section 2, we describe our observations, data reduction and imaging methods; in Section 3, we describe and analyse our source detection method and present our results; in Section 4, we describe the detected sources and discuss our analysis, and we summarize our results in Section 5.

2 OBSERVATIONS AND DATA REDUCTION

Observations of IC 10 were made using e-MERLIN (the upgraded Multi-Element Radio Linked Interferometer Network, an array consisting of seven radio telescopes spread across the UK¹) as part of LeMMINGs (Beswick et al. 2014), an e-MERLIN legacy project. The data were taken at two wavebands: 1.5 GHz (*L* band) and 5 GHz (*C* band) in four observing runs summarized in Table 2. The Lovell Telescope was available only for the 2016 February observation, resulting in a smaller field of view but higher sensitivity when compared to the other observing runs. The calibration and data reduction was carried out using AIPS,² following the calibration steps detailed in the e-MERLIN cookbook.³

2.1 Initial flagging and inspection

Before any calibration took place, we used SERPENT (Peck & Fenech 2013) with default settings to remove any obvious radio frequency interference (RFI). SERPENT is autoflagging software developed in PARSELTONGUE (Kettenis et al. 2006) principally for use in the e-MERLIN pipeline (Argo 2015). We also conducted further manual flagging to remove other obvious RFI that SERPENT had

missed. The visibilities from each data set were then visually inspected using the AIPS task IBLED to further identify and flag time periods when the data were corrupted. We estimate that overall, we are flagging ~ 52 per cent of the data at 1.5 GHz and ~ 10 per cent at 5 GHz.

2.2 1.5-GHz data

Both 1.5-GHz observations followed the same observational setup, which we describe here. The total bandwidth was split into eight IFs (intermediate frequencies), each with 128 individual channels of bandwidth 0.5 MHz. The primary flux calibrator, 3C 286, was used to set the flux scale, the point-like source, OQ208, was used to determine the passbands and relative antenna gains, and 0027+5958 was used as the phase calibrator. The observations started with 30-min scans of both the primary flux calibrator and point source, and then went on to alternate between observations of IC 10 and the phase calibrator, spending 5 min on IC 10 and 1 min on the phase calibrator each iteration. We followed standard calibration procedure to determine the complex gain solutions to apply to the data. The first and the last 15 channels in each IF were flagged because they are in the least sensitive areas of the passband and contribute mostly noise. Several rounds of phase-only self-calibration were carried out on the phase reference source and on IC 10 itself to improve the quality of the final maps. Each calibrated data set was weighted to give more weight to telescopes with a larger collecting area, improving sensitivity.

The Cambridge antenna was not available for the 2013 November observation, resulting in a slightly larger synthesized beam, as this antenna makes up the longest baselines in the e-MERLIN array. Additionally, IF 1 was flagged because no reliable flux density measurement for OQ208 could be obtained due to excessive RFI.

Both 1.5-GHz observations were calibrated independently and then combined. We verified that both data sets had the same flux scale by imaging eight bright sources within the primary beam but outside IC 10 (identified in preliminary imaging) and checking that the flux density measurements agreed to within 10 per cent error. The flux densities agreed for seven sources, showing that our flux scale is satisfactorily consistent between the observations. We conclude that the outlier must be due to variability between the observation dates. As the November data set was taken at a slightly higher frequency than the February data set, we used the AIPS task BLOAT to ensure that both observations covered the same frequency range before combining both data sets, using the task DBCON. The combined *uv* plane is displayed in Fig. 2(a).

2.3 5-GHz data

The 5-GHz observations followed an observing setup similar to the 1.5-GHz observations. The total bandwidth was split into four IFs, each with 128 individual channels 1 MHz wide. The primary flux calibrator, 3C 286, was used to set the flux scale, the point source, OQ208, was used to determine the passbands and relative antenna gains and 0027+5958 was used as the phase calibrator. IC 10 and the phase reference were observed alternately, with 5 min on IC 10 to 3 min on the phase calibrator, finishing with 30 min scans of both the primary flux and point source calibrators. The first and the last five channels were flagged because this is where the passband rapidly loses sensitivity. One round of phase-only self-calibration on IC 10 was performed to further improve the dynamic range of the final maps. Again, both calibrated data sets were weighted.

¹ A basic overview of the array can be found at <http://www.e-merlin.ac.uk/summary.html>

² AIPS, the Astronomical Image Processing Software, is free software available from the NRAO.

³ Available at: http://www.e-merlin.ac.uk/data_red/tools/e-merlin-cookbook_V3.0_Feb2015.pdf

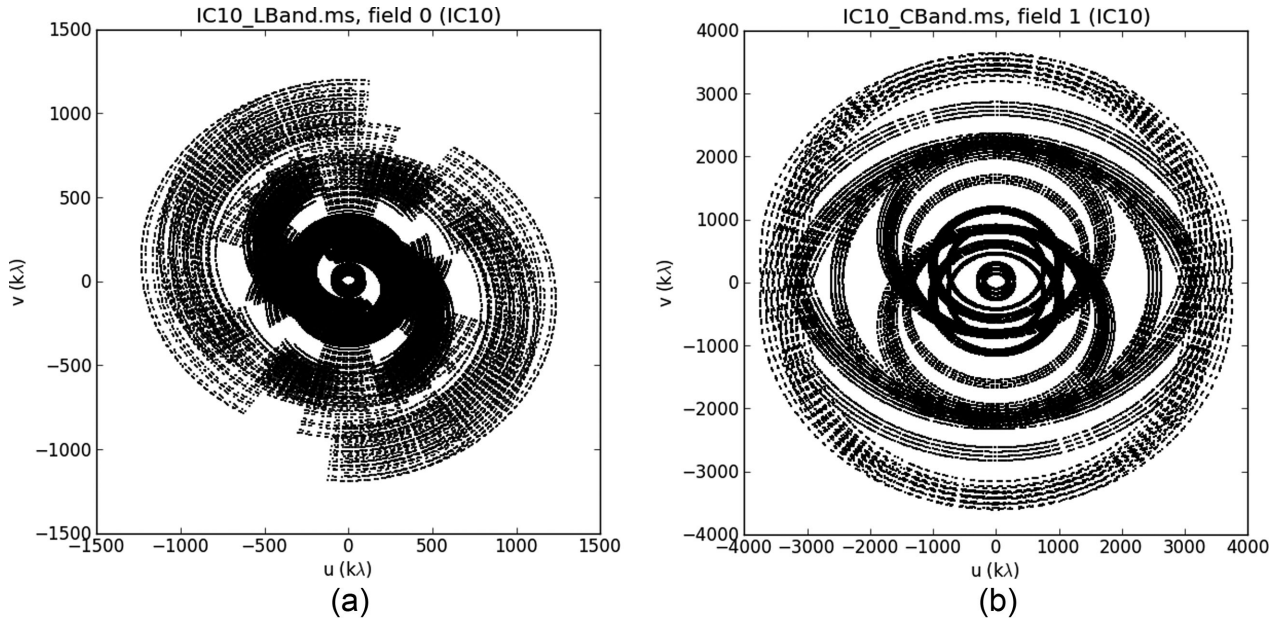


Figure 2. Distributions of visibilities in the uv planes for the e-MERLIN observations. (a) Shows the combined 1.5-GHz uv plane, and (b) shows the combined 5-GHz uv plane.

There were several issues with the 2016 February observation. The Mk2 antenna was not available for the duration of this observation and reliable gain solutions could not be found for the Darnhall antenna. The remaining data were combined with data taken in 2015 Apr to further reduce the noise level in the final maps. The combined 5-GHz uv plane is displayed in Fig. 2(b).

2.4 Imaging

IC 10's star-forming disc was imaged at 1.5 GHz with a mosaic of 19 subfields, with each subfield covering 0.3 arcmin a side. The AIPS task SETFC was used to generate the list of fields to be imaged and a natural weighting scheme was used to maximize sensitivity. A small field centred on the bright source NVSS002108+591132 was added to this list to remove its contaminating sidelobes. The individual subfields were cleaned down to 2.5 times the rms noise level of each map and were then mosaicked together using the AIPS task FLATN to produce a single widefield map of the entire disc. This widefield map was used to search for sources (see Section 3.1) and blank subfields with no apparent sources were used to test the widefield maps completeness (see Section 3.6). We image the detected sources separately at 5 GHz to save time, also using a natural weighting scheme to maximize sensitivity. We correct each detected source for the primary beam individually using the models described in Section 3.2. This was done to save time, as each detected source was sufficiently small to be characterized by a single primary beam correction factor.

Our final maps reach a noise level of $26 \mu\text{Jy beam}^{-1}$ at 1.5 GHz and $12 \mu\text{Jy beam}^{-1}$ at 5.0 GHz. These noise levels are significantly higher than the LeMMINGs target sensitivities of 8 and $3 \mu\text{Jy beam}^{-1}$ at 1.5 and 5 GHz, respectively. This can mainly be attributed to the lack of the Lovell Telescope in the majority of the presented observations as its inclusion results in a factor of 2 improvement in sensitivity (see e-MERLIN technical capabilities). Additionally, as the array was still in the commissioning phase for most of the observations, some antennas were not present for the entire duration of an observation. It is also likely that the increased

noise level is due to the considerable flagging carried out (see Section 2.1) and that low levels of unflagged RFI further contribute to the noise level in the final maps. Together, these factors largely explain the higher noise level. The sensitivity targets are likely to be hit in future LeMMINGs deep observations, provided that the Lovell Telescope will be included for the entire duration of these observations, and the e-MERLIN array will be operating at full capacity.

3 RESULTS

Radio emission from star-forming galaxies originates from two main sources, thermal emission from H II regions and non-thermal emission from cosmic ray electrons (CRE) that have been accelerated in SNR shock fronts. It is unlikely that any detections are related to X-ray binaries or planetary nebulae (Fender & Hendry 2000; Levens et al. 2016) as at the distance of IC 10, these sources would have flux densities of the order of $1 \mu\text{Jy}$. Very long baseline interferometers, such as e-MERLIN, effectively resolve out nearly all extended emission within observed galaxies, essentially highlighting compact star-forming products and contaminating background sources. In this section, we present our e-MERLIN detections within IC 10 and test the robustness of our detections.

3.1 Source detection

We used the widefield maps described in Section 2.4 to search for compact radio sources. We use the map at 1.5 GHz to search for sources, because not only does this map have a wider field of view, it is also more sensitive to extended emission than the corresponding 5-GHz maps (see Fig. 2). Furthermore, any sources dominated by non-thermal emission mechanisms will be brighter at 1.5 GHz due to the power-law radio spectra these sources exhibit. We used AEGEAN as our source extractor (Hancock et al. 2012) with a peak flux density threshold of five times the rms noise level, σ_{rms} , to find candidates. The source extractor retrieved 26 sources in total, of which 15 are coincident with IC 10's main disc. We cross-matched these remaining candidates with lower resolution features

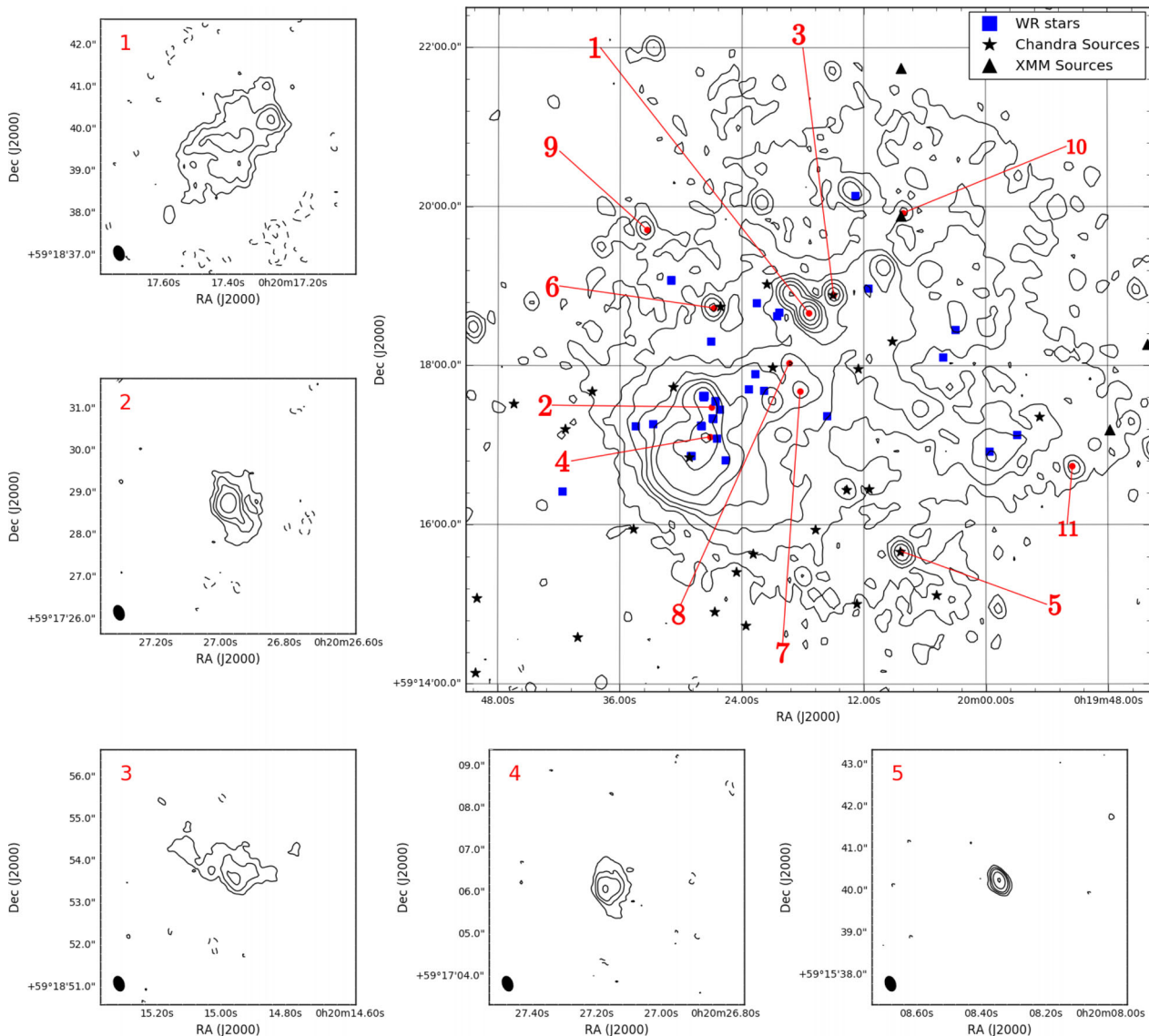


Figure 3. 1.5-GHz radio contours of IC 10. Top right: combined VLA C+D array map of IC 10 at 1.5 GHz, taken from Heesen et al. (2015). The contours are set to $-3, 5, 10, 20, 40, 80, 150, 300, 600 \times$ the $13 \mu\text{Jy beam}^{-1}$ noise level. The red numbers represent the locations of the detected e-MERLIN sources, the blue squares represent spectroscopically confirmed WR stars from Crowther et al. (2003), the black stars represent *Chandra* (resolution 3 arcsec) point source detections and the black upward triangles represent *XMM* (resolution 13 arcsec) point source detections. All X-ray data are taken from Wang, Whitaker & Williams (2005). The gridlines are the same as in Fig. 1. Surrounding plots: naturally weighted 1.5-GHz e-MERLIN detections from this study. The beam size for each image is $0.36 \text{ arcsec} \times 0.24 \text{ arcsec}$ and is displayed in the bottom-left corner of each map. The contours on each source are set to $-3, 3, 6, 10, 20, 40 \times$ the $26 \mu\text{Jy beam}^{-1}$ noise level. The contours also correspond to brightness temperatures set at 690, 1400, 2300, 4600 and 9200 K. Each field measures 6 arcsec a side. An identifying source number is located in the top-left corner of each contour map. Additional notes: the map of source 7 has been convolved to a resolution of twice the synthesized beam to show the low surface brightness emission. The contours on source 7 are set to the same levels as in the other contour maps, but the noise level in this case is $53 \mu\text{Jy beam}^{-1}$. The contours correspond to brightness temperatures set at 170 and 340 K in this case only.

from Karl G. Jansky Very Large Array (VLA) maps at 1.5 GHz (Heesen et al. 2015, see Fig. 3) to identify spurious detections. The lower resolution maps have a $13 \mu\text{Jy beam}^{-1}$ rms noise level, and so, we would expect to observe a 5σ e-MERLIN detection in these maps. We determine two of the e-MERLIN detections to be spurious and end up with a sample of 13 sources that we display in Fig. 3. The corresponding 5 GHz detections are displayed in Fig. 4. We discuss the completeness and reliability of our source detection method in Section 3.6.

3.2 Source flux measurement

We determine integrated flux densities for the unresolved and resolved sources using two different methods. For unresolved sources, we fit Gaussians through the use of the AIPS task JMFFIT. For resolved sources, we generate a mask by considering only emission associated with each source above a $3\sigma_{\text{rms}}$ level, where σ_{rms} is the local map rms noise level (measured off source). We then integrate the masked emission to find the integrated flux density.

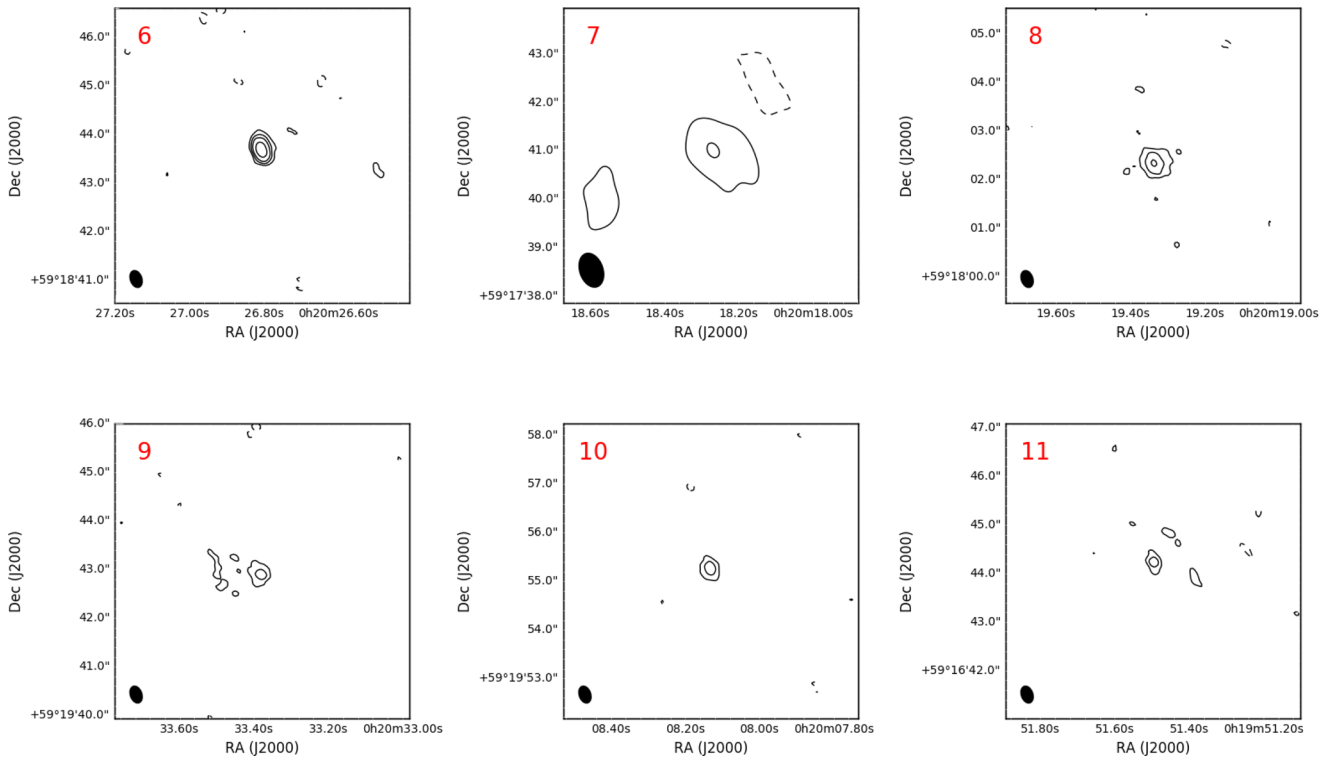


Figure 3 – continued

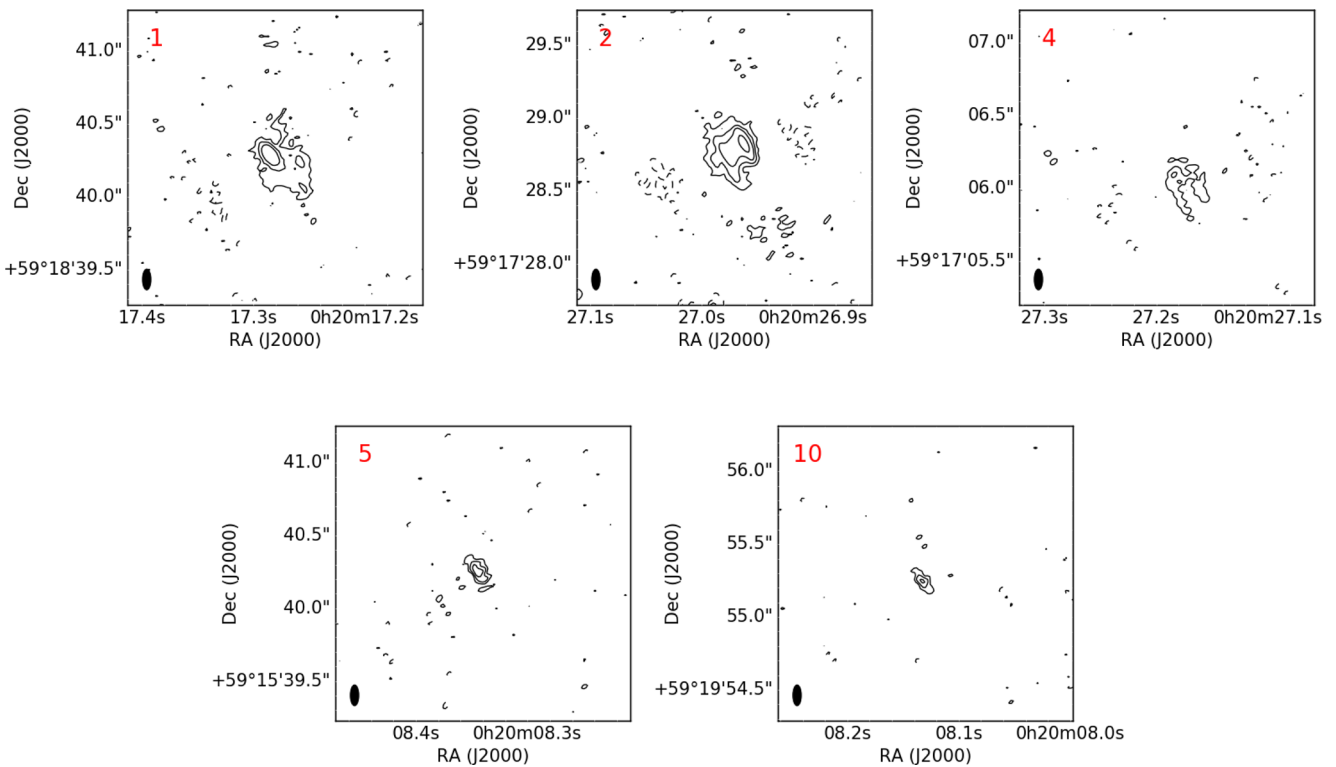


Figure 4. Naturally weighted 5-GHz e-MERLIN detections from this study. The beam size for this image is $0.14 \text{ arcsec} \times 0.06 \text{ arcsec}$ and is displayed in the bottom-left corner of each contour plot. The contours on each source are set to $-3, 3, 6, 10, 20, 40 \times$ the $12 \mu\text{Jy beam}^{-1}$ noise level. Each field measures 2 arcsec on a side. An identifying source number is located in the top-left corner of each contour map.

Table 3. Properties of sources detected in IC 10.

Source no.	IAU designation	α_{J2000} (h:m:s)	δ_{J2000} ($^{\circ}$: $'$: $''$)	$S_{1.5\text{ GHz}}$ (mJy)	$S_{5.0\text{ GHz}}$ (mJy)	Peak T_B (K)	Spectral index
1*	WBBH J002017+591839.7	00 20 17.390	+59 18 39.68	8.06 ± 0.82	1.02 ± 0.11	5200	<i>-0.3 ± 0.1</i>
2*	WBBH J002027+591728.7	00 20 26.952	+59 17 28.66	3.39 ± 0.35	2.28 ± 0.24	7700	<i>-0.1 ± 0.1</i>
3*	WBBH J002015+591853.9	00 20 14.988	+59 18 53.88	2.23 ± 0.25	–	2600	<i>-1.0 ± 0.1</i>
4*	WBBH J002027+591706.1	00 20 27.160	+59 17 06.12	1.83 ± 0.20	0.36 ± 0.06	4900	<i>-0.4 ± 0.1</i>
5	WBBH J002008+591540.2	00 20 08.348	+59 15 40.21	1.29 ± 0.14	0.28 ± 0.04	>11 000	-1.3 ± 0.2
6	WBBH J002027+591843.7	00 20 26.807	+59 18 43.69	0.99 ± 0.11	–	>8500	≤ -1.9
7*	WBBH J002018+591740.9	00 20 18.249	+59 17 40.92	0.93 ± 0.14	–	700	<i>-0.4 ± 0.1</i>
8	WBBH J002019+591802.3	00 20 19.334	+59 18 02.33	0.87 ± 0.16	–	>7700	≤ -2.0
9	WBBH J002033+591942.9	00 20 33.390	+59 19 42.89	0.49 ± 0.11	–	>4100	≤ -1.0
10	WBBH J002008+591955.2	00 20 08.137	+59 19 55.23	0.37 ± 0.07	0.14 ± 0.03	>3200	-0.8 ± 0.3
11	WBBH J001951+591644.2	00 19 51.498	+59 16 44.20	0.26 ± 0.06	–	>2000	≤ -1.1

Notes. Sources with superscript “*” are extended sources and their spectral indices (italicized) are derived from the low-resolution spectral index maps presented in Heesen et al. (2011). All other spectral indices are derived from the e-MERLIN observations. The peak brightness temperatures have been derived from the 1.5-GHz observations.

The errors for the integrated flux density measurements are determined using

$$\sigma_{\text{Total}} = \sqrt{(\sigma_{\text{Map}})^2 + (\sigma_{\text{Scale}})^2}, \quad (1)$$

where σ_{Map} is either equal to the fit error returned by JMFIT for unresolved sources or it is equal to $\sqrt{N}\sigma_{\text{rms}}$ for resolved sources (N is the number of independent beams that fit within the masked image). σ_{Scale} is the uncertainty in the flux scale, which is taken to be 10 per cent.

We correct the integrated flux density from each source for primary beam attenuation individually by assuming that the e-MERLIN primary beam can be parametrized by a Gaussian, as displayed in the e-MERLIN technical capabilities,⁴ with a full width at half-maximum (FWHM) of 30 arcmin for the 1.5-GHz observations (excluding the Lovell antenna) and a FWHM of 5.6 arcmin for the 5-GHz observations (including the Lovell antenna).

3.3 Brightness temperature

Assuming an optically thick source, the expected observed brightness temperature for free-free emission from H II regions is of the order of 10 000 K. Electrons radiating via non-thermal mechanisms, however, lead to observed brightness temperatures that can be much higher (e.g. 10^{12} K); brightness temperatures could therefore be used to aid in source classification.

Assuming a Rayleigh–Jeans blackbody curve, we calculate the brightness temperature, T_B , for each detected source using

$$T_B \approx \frac{c^2}{2\nu^2 k_B \Omega} \left(\frac{S_\nu}{10^{26} \text{ Jy W}^{-1} \text{ m}^2 \text{ Hz}} \right), \quad (2)$$

where k_B is the Boltzmann constant, c is the speed of light, ν is the central frequency of the combined 1.5-GHz observations (1518 MHz), Ω is the solid angle that the synthesized beam subtends and S_ν is the measured flux density in Jy. The derived brightness temperature is correct only for sources that are resolved, that is, when the synthesized beam is completely filled with the emitting source. As it stands, our brightness temperature for extended sources is likely to be an underestimate, due to us missing flux as a result of the lack of short baselines in these interferometric observations. The brightness temperature observed for unresolved sources will

Table 4. Angular sizes of extended and resolved sources at 1.5 GHz.

Source no.	Major axis ($'$)	Minor axis ($'$)	Position angle ($^{\circ}$)
1*	$3.34^{+0.30}_{-0.63}$	$1.85^{+0.26}_{-0.34}$	$138.96^{+13.37}_{-10.99}$
2*	$1.86^{+0.12}_{-0.34}$	$1.21^{+0.12}_{-0.27}$	$14.93^{+17.18}_{-19.65}$
3*	2.49 ± 0.38	$0.96^{+0.14}_{-0.29}$	$71.35^{+9.16}_{-6.76}$
4*	$1.46^{+0.09}_{-0.33}$	$0.90^{+0.04}_{-0.17}$	$9.51^{+11.49}_{-10.32}$
7*	$1.80^{+0.07}_{-0.21}$	$1.25^{+0.06}_{-0.20}$	$48.93^{+12.46}_{-11.37}$
8	0.694 ± 0.094	0.590 ± 0.080	123.65 ± 33.87

Notes. The superscript “*” in the source no. column indicates that the source is extended. The position angle of each source is measured anticlockwise from the north.

also be an underestimate, as the synthesized beam is larger than the true angular size of the source. Furthermore, our radio observations are probing optically thin conditions, resulting in a further reduction of the observed brightness temperatures. Therefore, the brightness temperatures derived for all sources should be treated as lower limits. We present the peak brightness temperature for each detected source in Table 3 and display brightness temperature contours for the resolved sources in Fig. 3.

3.4 Angular sizes

We measure the angular size, position angle and sky coordinates of each extended source by fitting an ellipse to the $3\sigma_{\text{rms}}$ contour. We optimize the fit by minimizing the χ^2 statistic, assuming that the error at each point on the contour is the same. We obtain errors in the fit via the $\Delta\chi^2$ method, that is, by modifying each individual parameter to gain χ^2 as a function of said parameter, whilst fixing all other parameters to the best fit. The quoted 1σ errors are defined by the intersect where $\Delta\chi^2$ from the minimized χ^2 is equal to 1.

For marginally resolved and unresolved sources, we fit 2D Gaussian functions using the AIPS task JMFIT to determine the angular size, position angle and sky coordinates. The angular size properties for extended and resolved sources at 1.5 GHz are summarized in Table 4, and the sky coordinates are presented in Table 3.

3.5 Spectral indices

Ideally, for an unambiguous source classification, we require a combination of reliable spectral indices ($S_\nu \propto \nu^\alpha$), to gain a measure of the spectral energy distribution for each compact source, and

⁴ Available at <http://www.e-merlin.ac.uk/tech/>

maps made at multiple epochs with a long enough time baseline to measure SNR expansion (~ 10 yr; McDonald et al. 2001; Beswick et al. 2006; Fenech et al. 2008).

These current observations are the highest resolution maps of IC 10 yet, and hence, we have no previous observations to observe any expansion. Furthermore, to recover reliable spectral indices for resolved sources, we require both observations to have significantly overlapping uv planes. For our current e-MERLIN observations however, this is not the case (see Fig. 2) and we can only gain reliable spectral indices for sources that are unresolved at both 1.5 and 5 GHz.

To find spectral indices for resolved sources, we make use of the spectral index maps provided in Heesen et al. (2011). These maps are taken at a much lower resolution than the presented e-MERLIN observations, and hence can only give us a general idea about the spectral index of the resolved sources combined with emission from their immediate surrounding environment.

3.6 Completeness and reliability

We carried out Monte Carlo simulations at 1.5 GHz to assess the completeness, C , and reliability, R , of our source detection method. At each band, we took a blank field from the widefield imaging (i.e. a noise map) and randomly added 400 Gaussian sources, each the same size as the naturally weighted synthesized beam. We assigned a flux density to each of these sources, drawn from a continuous, uniform probability distribution between 2 and 12 times the rms noise level of the maps. We then used AEGEAN to recover the placed sources, setting a detection threshold at three times the map rms noise level. As in our analysis, only sources exceeding a threshold

of 5σ are used to determine the statistical completeness of our source detection method. This process was repeated 1000 times to ensure a statistically robust answer.

We split our data into flux bins, each of width 0.5 times the map rms noise. We define the completeness and reliability for each flux bin as

$$C = \frac{N_M}{N_P} \quad (3)$$

$$R = \frac{N_M}{N_R}, \quad (4)$$

where N_M is the number of matched sources (a match is counted when the recovered source is spatially located within 1 synthesized beam of the placed source), N_P is the number of placed sources and N_R is the total number of matched sources recovered by the source extractor that also matched in flux (within $1\sigma_{\text{rms}}$ uncertainty). The completeness is essentially a measure of the fraction of real sources our source extractor detects and the reliability is a measure of how often spurious detections may be mistaken for real sources.

The results from this analysis are summarized in Fig. 5. We are complete down to approximately 7σ and reach 50 per cent completeness at approximately 5σ . The reliability plot tells us that our 5σ detections are very robust, and it is unlikely that any of these sources are spurious detections. Modifying the detection threshold results in a translation of the completeness distribution presented in the upper panel of Fig. 5, where the chosen threshold broadly matches when the completeness reaches 50 per cent. Changing the threshold to, for example, 3σ increases the completeness at low flux levels; however, this does not result in an increase in the reliability, as additional sources may be spurious.

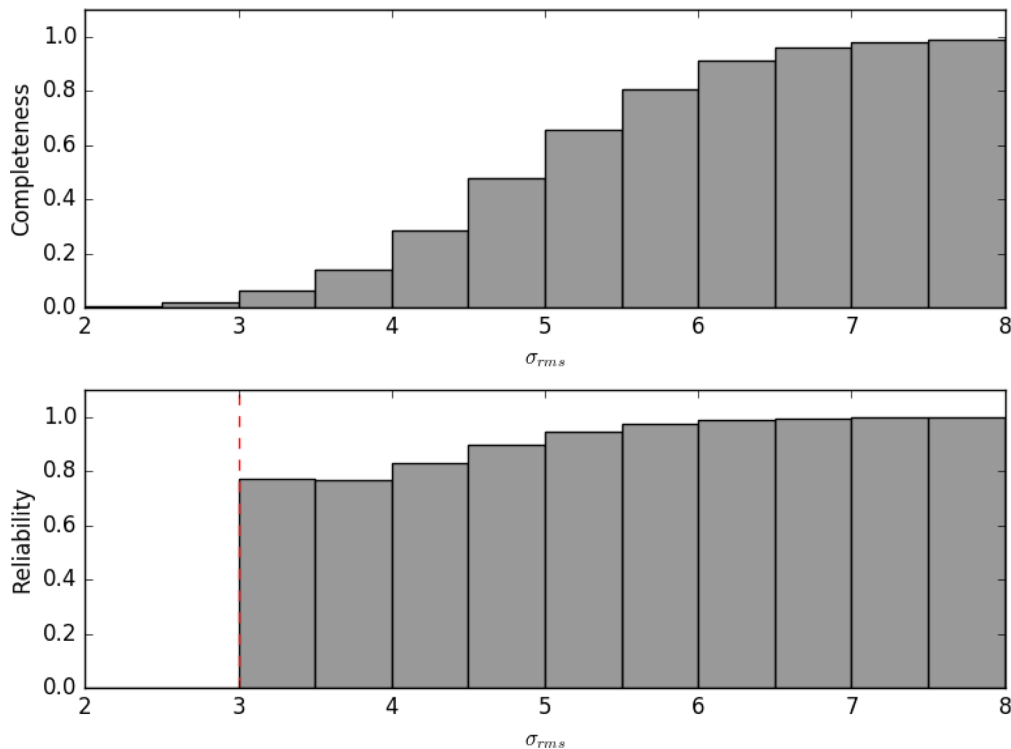


Figure 5. Completeness and reliability plots for the combined 1.5-GHz observations of IC 10. The uncertainty in all bins is < 5 per cent. In the lower plot, a vertical red dashed line represents the lower flux limit to which we can investigate the reliability.

4 DISCUSSION

4.1 Individual source notes

In this section, we briefly discuss each source in turn, highlighting relevant information to aid in its classification.

Source 1 (WBBH J002017+591839.7). This is the brightest source that we detect in our e-MERLIN observations, and it also has the largest angular size. There is evidence in the presented contour maps for a ‘clean bowl’, hinting that we are missing flux from this source due to the lack of short spacings in the e-MERLIN array. We find that this source is spatially coincident with emission peaks in the H α and 70- μ m maps as well as the lower resolution 5- and 1.5-GHz maps. This source also falls between two holes in the large-scale H I emission (see Fig. 1). We derive a brightness temperature of approximately 5000 K for this source, which is lower than expected. It is unlikely that this is due to a high optical thickness along the line of sight to the source, and is probably due to missing flux. The low-resolution spectral index from the literature is flat ($\alpha \sim -0.3$). In view of the above, we classify this source as a compact H II region within IC 10.

Source 2 (WBBH J002027+591728.7). This source is spatially coincident with peaks of emission in the H α and 70- μ m maps as well as the lower resolution 5- and 1.5-GHz maps. It is also spatially coincident with a current major star-forming region within IC 10 (Heesen et al. 2015), with numerous WR stars nearby. Moreover, this source is located within the highest peak of the H I distribution, indicating that SF is possibly being fuelled at this location. The low-resolution spectral index from the literature for this source is -0.1 , which is consistent with a dominating thermal contribution in this region. The brightness temperature for this source is of the order of 8000 K, which is roughly what is expected for an H II region. Therefore, it is likely that this source is a compact H II region within IC 10.

Source 3 (WBBH J002015+591853.9). This source is particularly interesting. It has an unusual extended morphology, no counterpart in either the H α or 70- μ m maps, and does not appear to be associated with any diffuse H I emission. This source does not appear to be related to any star-forming regions within IC 10, but it is spatially coincident with a *Chandra* X-ray source. As this source also has a steep low-resolution spectral index ($\alpha \sim -1.0$), determined from lower resolution maps in the literature, it is likely to be a contaminating background galaxy. This source has a lower than expected brightness temperature of roughly 3000 K, which could be due to high optical thickness along the line of sight to this source or due to missing flux from short baselines. Future VLA A-array 10-GHz observations would provide a reliable spectral index for this source and help determine whether it resides within IC 10.

Source 4 (WBBH J002027+591706.1). Like source 2, this source is coincident with emission in the H α and 70- μ m maps, the lower resolution 5- and 1.5-GHz maps as well as with a peak in the H I distribution. Source 4 is located on the outskirts of the NTSB (see Section 4.5), and there are many WR stars in this general region of the galaxy. We determine a brightness temperature of roughly 5000 K, which is lower than expected and could be due to the same reasons as discussed for source 1. This source has a relatively

flat low-resolution spectral index ($\alpha \sim -0.4$) and is likely to be a compact H II region within IC 10.

Source 5 (WBBH J002008+591540.2). This source is unresolved and located towards the southern outskirts of IC 10’s main disc. There are no corresponding sources at H α or 70 μ m. As this source is unresolved, the derived brightness temperature must be treated as a lower limit and the true brightness temperature must be greater than 10 000 K. If this source is of non-thermal origin, we expect that it must have an angular size much smaller than the synthesized beam. Furthermore, this source has a steep spectral index ($\alpha \sim -1.3$), as determined from our e-MERLIN observations, and it is also coincident with a *Chandra* X-ray source. It is likely that this source is a background AGN.

Source 6 (WBBH J002027+591843.7). This source is unresolved and located towards the north-east of IC 10’s main disc. Similarly to source 5, there is no corresponding emission in either H α or 70- μ m maps. We derive a lower limit for the brightness temperature of 8000 K, but this is likely to be due to the source filling a small fraction of the synthesized beam. This source is spatially located close to but separate from a *Chandra* X-ray source. It is surprising that we do not detect this bright source in the presented 5-GHz observations, resulting in an extremely steep spectral index estimate ($\alpha \leq -1.9$). From this evidence, it is likely that this source is a background source.

Source 7 (WBBH J002018+591740.9). This source has a resolved, diffuse structure with a sharp peak above the $5\sigma_{\text{rms}}$ threshold. In Fig. 3, we display a contour map that we convolved to a resolution of twice the naturally weighted synthesized beam to highlight this diffuse emission. We carried out the same analysis as for the other sources but with a beam that was twice the size. The peak brightness temperature for this source was found to be just 700 K, and this should be treated as a lower limit. This source is located roughly in the centre of IC 10’s main disc, with corresponding peaks of emission in the H α , 70- μ m and the low-resolution radio continuum maps. Moreover, this source has a flat low-resolution spectral index, suggesting that this source is possibly an H II region within IC 10, although more investigation will be required to fully classify this source. There is emission at a $3\sigma_{\text{rms}}$ level located ~ 2.5 arcsec towards the south-east of this source. If this emission is also associated with source 7, it is possible that this source is a young SNR and we are observing high brightness features in the expanding shell (see Section 4.4). Future, more sensitive, e-MERLIN 1.5-GHz and VLA 1.5-GHz A-array observations will be required to determine if this source has an extended component. VLA 10-GHz A-array observations could also be used to derive a resolved spectral index to aid in classifying this source.

Source 8 (WBBH J002019+591802.3). This source is partially resolved and located towards the centre of IC 10. This source is coincident with diffuse emission in the H α map, and with peaks in the 70- μ m and low-resolution radio maps. We do not detect this source in the presented 5-GHz maps, resulting in a very steep inferred spectral index ($\alpha \leq -2.0$). We present a lower limit for the brightness temperature of the order of 8000 K. This source could either be a background source or a peak in a more extended H II region. Deeper e-MERLIN 5-GHz observations would be required

to obtain a reliable spectral index for this source and to determine its membership to IC 10.

Source 9 (WBBH J002033+591942.9). This source is another compact, unresolved source located towards the north-east of IC 10's main disc. The source appears to be extended to the east in Fig. 3, but visual inspection suggests this to be a noise peak. This source appears isolated from IC 10's main disc, with no corresponding emission in either the $H\alpha$ or 70- μm maps. This source is faint with a lower limit to the brightness temperature of 4000 K, which is probably due to the source filling a small fraction of the synthesized beam. Due to its isolation, we classify this source as a background galaxy.

Source 10 (WBBH J002008+591955.2). This source is another unresolved source located towards the north-west of IC 10's main disc. This source looks like it could be associated with the northern ring in the $H\text{I}$ distribution (see Fig. 1), but it appears to be an offset. There is no corresponding emission in either $H\alpha$ or 70- μm maps. We derive a lower limit to the brightness temperature of 3000 K, which is possibly due to the source filling a small fraction of the synthesized beam. This source appears to be coincident with a low-resolution *XMM* X-ray source, but due to the low resolution (13 arcsec; Wang et al. 2005), we cannot say with certainty that this source is the origin of the X-ray emission. This current evidence suggests that this source is a faint background source.

Source 11 (WBBH J001951+591644.2). This source is another faint, unresolved source that is located towards the west of IC 10's main disc. This source falls within extended emission in the 70- μm map, but the $H\alpha$ map does not extend this far. This source is likely to be a background galaxy, as it has a steep spectral index ($\alpha < -1.1$) and there are no coincident compact sources at any other wavelength. It could also be a peak in a more diffuse $H\text{II}$ region, but this is unlikely given the spectral index. The lower limit to the brightness temperature is still quite low (~ 2000 K), which is possibly due to the source filling a small fraction of the synthesized beam. Further investigation will be required to properly classify this source, but current evidence indicates it is likely to be a background galaxy.

4.2 Expected background source count

We derive the expected number of background sources coincident with IC 10 by analysing source counts from the literature. We fit the source counts from Massardi et al. (2010) with a fourth-order polynomial.⁵ This was chosen as it is the lowest order polynomial that represents the data well. We then apply corrections for completeness (see Section 3.6) and end up with an estimate for the background count of 14.8 ± 3.8 sources in a circular field of radius 5 arcmin. It is likely that this estimate is a slight overestimate as any nearby extended sources will be resolved out, but this is expected to affect only brighter sources that contribute little to the overall counts. In a region of the same size centred on IC 10 (see Section 3.1), we detect 15 sources, which is consistent with the hypothesis that all detected sources are background galaxies. As discussed in Section 4.1, it is clear from comparison with $H\alpha$ and 70- μm maps that at least three of our detections reside within IC 10,

⁵The raw data are available from http://web.oapd.inaf.it/rstools/srcnet/srcnet_tables.html

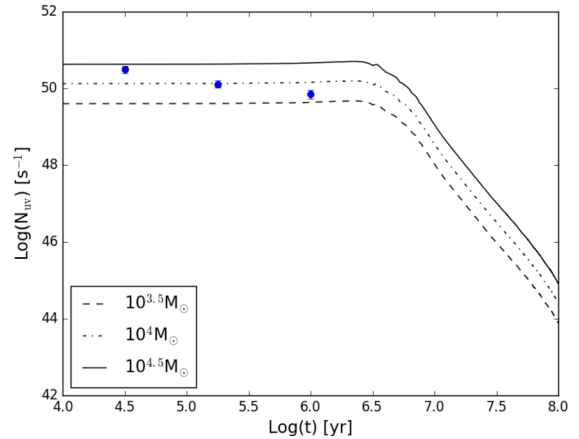


Figure 6. *STARBURST99* models of the Lyman continuum production rate as a function of time for three cluster masses. The solid line represents a $10^{4.5} M_{\odot}$ cluster, the dot-dashed line represents a $10^4 M_{\odot}$ cluster and the dashed line represents a $10^{3.5} M_{\odot}$ cluster. We plot the lower limits for the Lyman continuum production rate for sources 1, 2 and 4 (blue dots). Note that we do not know the age of the observed $H\text{II}$ regions and so the position on the time axis was arbitrarily chosen to clearly identify where each source lies with respect to the constant Lyman continuum production phase.

but it is obvious from this exercise that the majority of the detected sources are probably background galaxies.

4.3 Compact $H\text{II}$ regions within IC 10

From our discussion in Section 4.1, we determined that sources 1, 2 and 4 are likely to be compact $H\text{II}$ regions within IC 10. The source of the ionizing Lyman continuum photons that produce these $H\text{II}$ regions is the young massive O- and B-type stars (Strömgren 1939). If we assume that all detected radio emission from these sources at 1.5 GHz is thermal in origin, we can calculate the production rate of Lyman continuum photons required to produce the observed radio emission. By comparing these results with the outputs from stellar population synthesis models, we can determine an estimate for the total stellar mass contained within the star clusters responsible for the observed $H\text{II}$ regions.

To estimate the total production rate of Lyman continuum photons for each detected compact $H\text{II}$ region, we applied equation 2 from Condon (1992), assuming an electron temperature of 10^4 K. These estimates will be lower limits for the true Lyman continuum production rate, as not only are we resolving out some of the extended emission associated with these sources, some Lyman continuum photons may also be absorbed by dust within the $H\text{II}$ regions themselves. We then used *STARBURST99* (Leitherer et al. 1999) to produce models for the Lyman continuum production rate as a function of time for various stellar cluster masses. We assume a Miller–Scalo IMF (Miller & Scalo 1979) that all SF takes place in a single instantaneous burst at $t = 0$, and that all stars larger than $8 M_{\odot}$ explode as SNe. We also assume Geneva evolutionary tracks with standard mass-loss at a metallicity of $Z = 0.004$ (Charbonnel et al. 1993), as this metallicity closely reflects that observed for IC 10 (Garnett 1990; Leroy et al. 2006).

Each of the models for the Lyman continuum production rate has the same shape, the production rate is constant for the first $\sim 10^{6.5}$ yr before sharply declining due to the massive stars that produce the Lyman continuum emission exploding as SNe (see Fig. 6). As we do not know the age of the observed $H\text{II}$ regions, we do not know if any of the massive OB stars have already exploded as SNe. However,

Table 5. Determined H II region properties.

Source	N_{UV}	Stellar cluster mass	# SNe
1	$\geq 3.1 \times 10^{50} \text{ s}^{-1}$	$\geq 22\,000 M_{\odot}$	$\gtrsim 266$
2	$\geq 1.3 \times 10^{50} \text{ s}^{-1}$	$\geq 9500 M_{\odot}$	$\gtrsim 115$
4	$\geq 7.0 \times 10^{49} \text{ s}^{-1}$	$\geq 5200 M_{\odot}$	$\gtrsim 63$

Notes. # SNe is the total number of expected SNe over the entire lifetime of the H II region assuming a Miller–Scalo IMF with all stars greater than $8 M_{\odot}$ exploding as SNe.

as these sources are also observable in the H α map (see Fig. 1), it is likely that no SNe have yet disrupted the Lyman continuum production rate, and that we are observing these H II regions in the early constant production phase. Comparing our observed Lyman continuum production rate with the constant phase predicted from STARBURST99 will therefore give a reasonable estimate of the lower limit for the stellar cluster mass.

We determine the stellar masses for each detected H II region by interpolating between the constant production phase for each STARBURST99 model. The derived lower limits for the cluster masses along with the total number of expected SNe originating from these clusters are presented in Table 5. These estimates do not vary much with assumed metallicity, but do vary greatly with assumed IMF. Rerunning the simulations again assuming solar metallicity results in a 5 per cent increase in the cluster mass; however, rerunning the simulations assuming a Salpeter IMF (Salpeter 1955) results in a 50 per cent decrease in the cluster mass. The derived cluster mass for sources 1 and 2 is larger than the average stellar cluster found within the Large Magellanic Cloud (LMC), whereas source 4 reflects a more typical cluster mass (Hunter et al. 2003). For reference, the derived cluster mass for source 1 is approximately half that of 30 Doradus in the LMC (Hunter et al. 1995; Andersen et al. 2009).

4.4 SNR within IC 10

Although we cannot individually classify with confidence all detected sources within IC 10, we can use the source sizes and evolution time-scales from the literature to constrain how many SNR we would expect to detect. It is useful to utilize observations of the LMC and Small Magellanic Cloud, as these galaxies have similar environmental properties similar to IC 10 and are nearby, allowing for more complete studies of their SNR populations.

Studies of the SNR in the Magellanic clouds (see reference list in Filipović & Bozzetto 2016) reveal that the average size of an SNR is ~ 40 pc (Filipović & Bozzetto 2016), which is similar to the average size of SNR in M33 (Long et al. 2010) and M31 (Lee & Lee 2014). Scaling to our assumed distance of 0.7 Mpc, we would expect an average SNR to have an angular size of ~ 12 arcsec. e-MERLIN essentially begins to resolve out sources that have an angular size larger than 2 arcsec at 1.5 GHz.⁶ A rough calculation using equations detailed in Draine (2011) reveals that SNR appearing to be 2 arcsec in size would be ~ 40 yr in age and still in the short-lived free expansion phase (Draine 2011). As most observed SNR are in the Sedov–Taylor phase of expansion (which remains observable for $\sim 10^4$ yr; Strong, Moskalenko & Ptuskin 2007), even with a large sample of SNR, we would expect only a small fraction to be young SNR. It is therefore likely that we are resolving out most of the SNR

within IC 10. We are, however, still sensitive to high brightness features within an expanding SNR shell, and so it is possible that some of our observed sources are part of an expanding SNR shock fronts.

Through measurements of the integrated SFR of IC 10, we can gain an approximate estimate of the number of observable SNR that we would expect to find using high-resolution radio continuum observations. Following the calculations carried out in Condon (1992), assuming a Miller–Scalo IMF (Miller & Scalo 1979) with all stars with mass above $8 M_{\odot}$ exploding as SNe and using the SFR from Hunter et al. (2012), we find that the SN rate is approximately $\nu_{\text{SN}} = 8.1 \times 10^{-4} \text{ yr}^{-1}$. With a typical lifetime of 10^4 yr, one would expect to observe roughly 8 SNR. Brighter radio SNe (RSNe) are observable for a much shorter time period (~ 10 yr; Stockdale et al. 2001; Weiler et al. 2002), and so it is very unlikely that we will detect any RSNe in IC 10 at all.

There are other biases that will affect the detectability of SNR. For example, synchrotron emission requires magnetic fields to produce emission. Magnetic fields are amplified in SNR shock fronts (Guo et al. 2012) and the base magnetic field strength is related to the density of the surrounding gas (Vallée 1995; Niklas & Beck 1997). As the gas density in dwarf galaxies is low, we expect an SNR within IC 10 to be intrinsically fainter than those taking place in denser environments (such as M82 and Arp 220).

As we expect to find so few SNR in general, it is unlikely that we are observing any young SNR with these e-MERLIN observations. Instead, we are more likely to be observing compact H II regions and background sources. In general, e-MERLIN would be well suited to observe SNR at 1.5 GHz in galaxies at distances > 4 Mpc. At this distance, the average SNR would appear ~ 2 arcsec in size and the SNR would not be resolved out due to the long baselines in the e-MERLIN array. For galaxies that are closer than 4 Mpc, e-MERLIN observations should be combined with VLA A-array observations, which will provide the required sensitivity to large-scale emission in order to identify possible SNR within these galaxies.

4.5 Non-thermal superbubble

The NTSB within IC 10 (Yang & Skillman 1993) is a remarkable example of SN feedback in a low-density environment. The NTSB is adjacent to the largest current star-forming site in IC 10 and at its centre resides one of the most massive stellar mass black holes ever discovered (IC 10 X–1, $\geq 23.1 M_{\odot}$; Silverman & Filippenko 2008). There is diffuse X-ray emission in this area of the galaxy, which is similar to 30 Doradus in the LMC (Wang 1999; Wang et al. 2005). It has been speculated that this black hole is the remains of a hypernova that is responsible for the NTSB (Lozinskaya & Moiseev 2007), although it has been argued that the superbubble could be the result of a collection of many ordinary SNe (Yang & Skillman 1993). The NTSB is dominated by emission of non-thermal origin, and the presence of an H I ‘bubble’ in this region presents evidence that there possibly exists a cavity in the interstellar medium (ISM) at this location (Heesen et al. 2015).

We do not see any compact radio sources within the NTSB in the e-MERLIN observations. We would not expect to see any SNe in this region due to the arguments given in Section 4.4, and this hypothesis can be further supported by considering the environmental conditions within the NTSB. The initial growth of superbubbles in general is thought to originate from the winds of massive stars that rarify their immediate environment (Krause et al. 2013). As these stars explode as SNe, their shockwaves will quickly propagate through the rarified ISM until they reach the outer, dense

⁶ See e-MERLIN Cycle 4 capabilities available at <http://www.e-merlin.ac.uk/observe/cycle4.html>

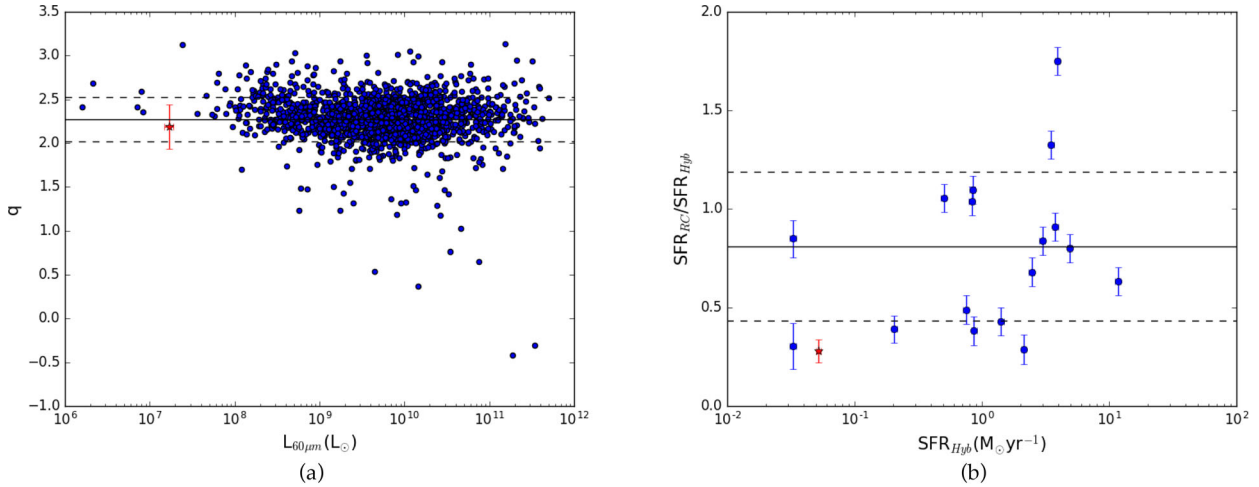


Figure 7. (a) Distribution of q values plotted as a function of *IRAS* 60- μm luminosity. The blue points are taken from Yun, Reddy & Condon (2001) and the red star presents IC 10’s location. The solid line represents the mean q value for the sample and the dotted lines present the 1σ deviations from the mean. (b) Ratio of the radio continuum SFR determined via the Condon relation (Condon 1992) to the Hybrid SFR as a function of Hybrid SFR for the Heesen et al. (2014) sample. The red star presents IC 10’s location. The solid line represents the mean of the sample excluding dIrr galaxies and the dotted lines represent 1σ deviations from the mean.

superbubble shell where they can more efficiently accelerate CRE and produce substantial radio emission. Hence, we would expect to see a large radio ‘shell’ surrounding the NTSB where the SNE shock fronts essentially catch up with the edge of the superbubble.

It is interesting that we do not resolve a shock front associated with the NTSB in these high-resolution observations. This could simply be due to the interferometer resolving out large-scale emission (the NTSB itself is ~ 50 arcsec across); however, we would expect to see features in the shell that are smaller than 2 arcsec. It is also possible that the expansion of the superbubble has slowed sufficiently such that CRE cannot be effectively accelerated via the diffusive shock acceleration process in the expanding shell (Longair 2011). Recent estimates of the dynamical age and expansion velocity of the superbubble from Heesen et al. (2015) suggest that the latter is likely and that the NTSB could be in a ‘fade-out’ stage of its evolution.

4.6 Updated integrated flux measurement

The radio–FIR relation is a very tight trend that holds over four orders of magnitude in luminosity (e.g. Yun et al. 2001), linking both radio continuum and FIR emission to massive SF. Dwarf irregular galaxies are found to lie on this correlation, yet they are observed to have a deficiency in radio continuum when compared to the SFR derived from hybrid SF tracers (Kitchener et al. 2015). The reason for this deficiency is interpreted to be due to CRE escaping from their low gas density environments (Klein, Weiland & Brinks 1991; Lacki et al. 2010; Kitchener et al. 2015), which needs to be coupled with escaping far-UV photons to explain their location on the radio–FIR relation (the radio–FIR conspiracy; Lacki et al. 2010).

Total flux measurements of galaxies are typically determined through single dish observations, which are often contaminated by background sources. As dwarf irregular galaxies are intrinsically faint in radio continuum, the background sources could dominate the observed radio emission, resulting in an incorrect measurement of the total radio emission from the galaxy itself. With this current study, we identify potential background sources and use our high-resolution maps to update the integrated flux density measurements in the literature accordingly.

We use the measurements from Chyży et al. (2016), which are 377 ± 11 mJy at 1.43 GHz and 222 ± 9 mJy at 4.85 GHz, as the integrated flux measurements for IC 10. These measurements have already been corrected for the presence of four background sources that are observed in the halo of the galaxy, but not for the existence of background sources within the main star-forming disc. We use our high-resolution e-MERLIN maps to identify background sources within IC 10’s main disc, but measure the total flux density for these sources from lower resolution VLA maps presented in Heesen et al. (2015). The e-MERLIN sources can easily be identified in the lower resolution VLA maps and by using this method, we minimize the amount of flux that we miss due to missing short spacings.

As the VLA maps were taken at 1.5 and 6 GHz, we use the spectral index between the Chyży et al. (2016) measurements ($\alpha = -0.43 \pm 0.09$) to find the expected integrated flux densities at these frequencies. We then measure the flux density of sources that are determined to be background sources from the VLA maps using the AIPS task JMFIT. We subsequently subtract these sources (sources 3, 5, 6, 9 and 10) along with four additional faint sources detected in IC 10’s halo to obtain a corrected flux density of 352 ± 11 mJy at 1.5 GHz and 199 ± 9 mJy at 6 GHz.

Subtracting the contaminating background sources in IC 10’s main disc results in only a 4 per cent decrease in the flux density at 1.5 GHz and a 2 per cent decrease at 6 GHz. Contaminating background sources do not contribute significantly to the overall flux density measured from IC 10 at radio wavelengths, and previous analysis concerning its integrated properties remains valid.

We combine this updated radio flux density with *IRAS* 60- and 100- μm flux densities taken from Fullmer & Lonsdale (1989) to find $q_{\text{IC10}} = 2.19 \pm 0.25$. The q parameter is essentially a measure of the radio–FIR relation and is defined in Condon, Anderson & Helou (1991) as

$$q = \log \left(\frac{\text{FIR}}{3.75 \times 10^{12} \text{ W m}^{-2}} \right) - \log \left(\frac{S_{1.4\text{GHz}}}{\text{W m}^{-2} \text{ Hz}^{-1}} \right) \quad (5)$$

$$\text{FIR} = 1.26 \times 10^{-14} (2.58 S_{60\mu\text{m}} + S_{100\mu\text{m}}) \text{ W m}^{-2}, \quad (6)$$

where $S_{60\mu\text{m}}$ and $S_{100\mu\text{m}}$ are the *IRAS* 60- and 100- μm flux densities measured in Jy. It is clear from Fig. 7(a) that IC 10 lies within 1σ of

the radio–FIR relation found for more massive star-forming galaxies (Yun et al. 2001). This result agrees with earlier authors who find that low-luminosity dwarf galaxies continue to follow the radio–FIR relation (Chyży et al. 2011; Roychowdhury & Chengalur 2012).

We also transform the updated radio flux measurement to an SFR via the Condon relation (Condon 1992) and compare this with the SFR measured from hybrid SF tracers ($0.052 \pm 0.003 M_{\odot} \text{ yr}^{-1}$; Heesen, private communication) to find that IC 10 lies just below the radio–SFR relation from Heesen et al. (2014, see Fig. 7b). We would expect IC 10 to be radio deficient due to the escape of CRE in a galactic wind (Chyży et al. 2016), yet it is interesting to note that this does not result in a significant deviation from the radio–SFR relation. We cannot currently say whether IC 10 is an example of the radio–FIR ‘conspiracy’ as the sample size used to determine the radio–SFR relation is small with a large scatter. Future studies with a larger sample would reveal the true significance of the deviation.

5 CONCLUSIONS

We present high-resolution e-MERLIN observations of the nearby dwarf irregular galaxy IC 10 as a part of the LeMMINGs project. Our main conclusions are as follows.

(i) Our e-MERLIN observations reveal 11 compact radio sources at 1.5 GHz coincident with IC 10’s star-forming disc, five of which also have detections at 5 GHz. Although we cannot conclusively classify all sources on the basis of their spectral index due to differences in sampling the uv plane, we gain insight into the nature of each source through the use of low-resolution multiwavelength data, the positional coincidence with features at other wavelengths such as H α and 70 μm , and an estimate of their brightness temperature.

(ii) Based on our analysis of the expected background source counts, the number of detected sources is consistent with them all being background sources. However, as some sources closely trace compact emission in maps at other wavelengths, giving us confidence that some of these sources do in fact belong to IC 10. We find that of the 11 sources, three likely reside in IC 10 (sources 1, 2 and 4), all of which are H II regions; five are background sources (sources 3, 5, 6, 9, 10) and three are yet to be conclusively classified (sources 7, 8, 11).

(iii) Based on the time-scale over which SNR are typically observable and the resolution limitations of these high-resolution interferometry observations, we expect that we will not be able to detect any SNR with the present e-MERLIN observations. The only SNe we would expect to be able to detect are very young RSNe, but it is unlikely that we would observe any due to a combination of their short observable time-scales and low SFR observed in IC 10. We explore other possible factors that could affect SNR detectability in dwarf irregular galaxies and conclude that e-MERLIN alone is well suited to study SNR in galaxies located at distances greater than 4 Mpc due to the spatial frequencies covered by the array. For galaxies closer than 4 Mpc, additional VLA observations are required to fully cover the spatial scales that SNR candidates occupy.

(iv) The same reasons as mentioned above explain why we see no compact sources within the NTSB in IC 10 and that the detected sources that belong to IC 10 are likely to be compact H II regions. Based on STARBURST99 models, we determine lower limits for the stellar cluster masses required to produce these observed compact H II regions; the largest one is about half the size of 30 Doradus in the LMC.

(v) We present updated integrated flux densities for IC 10, where we subtract the contribution from background sources from liter-

ature data. We find a 4 per cent reduction in the measured flux at 1.5 GHz and a 2 per cent reduction at 4.85 GHz.

(vi) With this updated measurement, we find that IC 10 lies below the radio–SFR relation derived in (Heesen et al. 2014), yet still remains on the radio–FIR relation. Further studies with larger samples are required to place significance on IC 10’s radio deficiency to determine whether it is an example of the radio–FIR ‘conspiracy’.

Further observations are required to fully classify the observed resolved sources. Ideally, VLA A-array observations taken at 10 GHz will match the uv coverage of the current 1.5-GHz observations and allow for reliable spectral indices for all detected sources to be determined and further A-array observations at 1.5 GHz will aid in the detection of SNR.

Regarding future LeMMINGs deep targets, 10-GHz A-array VLA observations for all targets would greatly aid in classifying detected compact sources, whereas 1.5-GHz A-array VLA observations would be necessary only for targets that are located closer than ~ 4 Mpc to improve sensitivity to more extended emission.

Because of the low integrated SFR of individual dIrr galaxies, observations suffer from low-number statistics. In order to make progress, rather than targeting individual dIrr systems, an ensemble would need to be observed and statements made on a statistical basis. In contrast, larger star-forming spiral and starburst galaxies will contain many more compact sources and could be analysed on a galaxy-by-galaxy basis; it is suggested the next phase of LeMMING should place its focus there.

ACKNOWLEDGEMENTS

JW acknowledges support from the UK’s Science and Technology Facilities Council [grant number ST/M503514/1].

EB acknowledges support from the UK’s Science and Technology Facilities Council [grant number ST/M001008/1].

VH acknowledges support from the UK’s Science and Technology Facilities Council [grant number ST/J001600/1].

e-MERLIN is a National Facility operated by the University of Manchester at Jodrell Bank Observatory on behalf of STFC.

PARSELTONGUE was developed in the context of the ALBUS project, which has benefited from research funding from the European Community’s sixth Framework Programme under RadioNet R113CT 2003 5058187.

REFERENCES

- Andersen M., Zinnecker H., Moneti A., McCaughrean M. J., Brandl B., Brandner W., Meylan G., Hunter D., 2009, *ApJ*, 707, 1347
 Appleton P. N. et al., 2004, *ApJS*, 154, 147
 Argo M., 2015, *J. Open Res. Softw.*, 3, p.e2
 Ashley T., Elmegreen B. G., Johnson M., Nidever D. L., Simpson C. E., Pokhrel N. R., 2014, *AJ*, 148, 130
 Bauer F. E., Brandt W. N., 2004, *ApJ*, 601, L67
 Bell E. F., 2003, *ApJ*, 586, 794
 Beswick R. J. et al., 2006, *MNRAS*, 369, 1221
 Beswick R., Argo M. K., Evans R., McHardy I., Williams D. R. A., Westcott J., 2014, *Proc. Sci.*, LeMMINGs e-MERLIN Survey of Nearby Galaxies. SISSA, Trieste, PoS(EVN 2014)010
 Brandt W. N., Ward M. J., Fabian A. C., Hodge P. W., 1997, *MNRAS*, 291, 709
 Charbonnel C., Meynet G., Maeder A., Schaller G., Schaerer D., 1993, *A&AS*, 101, 415
 Chyży K. T., Weżgowiec M., Beck R., Bomans D. J., 2011, *A&A*, 529, A94
 Chyży K. T., Drzazga R. T., Beck R., Urbanik M., Heesen V., Bomans D. J., 2016, *ApJ*, 819, 39

- Condon J. J., 1992, *ARA&A*, 30, 575
- Condon J. J., Anderson M. L., Helou G., 1991, *ApJ*, 376, 95
- Crowther P. A., Drissen L., Abbott J. B., Royer P., Smartt S. J., 2003, *A&A*, 404, 483
- Demers S., Battinelli P., Letarte B., 2004, *A&A*, 424, 125
- Draine B. T., 2011, *Physics of the Interstellar and Intergalactic Medium*. Princeton Univ. Press, Princeton, NJ
- Fender R. P., Hendry M. A., 2000, *MNRAS*, 317, 1
- Fenech D. M., Muxlow T. W. B., Beswick R. J., Pedlar A., Argo M. K., 2008, *MNRAS*, 391, 1384
- Filipović M. D., Bozzetto L. M., 2016, preprint ([arXiv:1604.01458](https://arxiv.org/abs/1604.01458))
- Fullmer L., Lonsdale C. J., 1989, *Cataloged Galaxies and Quasars Observed in the IRAS Survey*. Jet Propulsion Laboratory, Pasadena
- Garnett D. R., 1990, *ApJ*, 363, 142
- Guo F., Li S., Li H., Giacalone J., Jokipii J. R., Li D., 2012, *ApJ*, 747, 98
- Hancock P. J., Murphy T., Gaensler B. M., Hopkins A., Curran J. R., 2012, *MNRAS*, 422, 1812
- Heesen V., Rau U., Rupen M. P., Brinks E., Hunter D. A., 2011, *ApJ*, 739, L23
- Heesen V., Brinks E., Leroy A. K., Heald G., Braun R., Bigiel F., Beck R., 2014, *AJ*, 147, 103
- Heesen V. et al., 2015, *MNRAS*, 447, L1
- Hodge P., Lee M. G., 1990, *PASP*, 102, 26
- Hunter D. A., 2001, *ApJ*, 559, 225
- Hunter D. A., Elmegreen B. G., 2004, *AJ*, 128, 2170
- Hunter D. A., Shaya E. J., Holtzman J. A., Light R. M., O’Neil E. J., Jr, Lynds R., 1995, *ApJ*, 448, 179
- Hunter D. A., Elmegreen B. G., Dupuy T. J., Mortonson M., 2003, *AJ*, 126, 1836
- Hunter D. A. et al., 2012, *AJ*, 144, 134
- Jarrett T. H., Chester T., Cutri R., Schneider S. E., Huchra J. P., 2003, *AJ*, 125, 525
- Kettenis M., van Langevelde H. J., Reynolds C., Cotton B., 2006, in Gabriel C., Arviset C., Ponz D., Enrique S., eds, *ASP Conf. Ser. Vol. 351, Astronomical Data Analysis Software and Systems XV*. Astron. Soc. Pac., San Francisco, p. 497
- Kim M., Kim E., Hwang N., Lee M. G., Im M., Karoji H., Noumaru J., Tanaka I., 2009, *ApJ*, 703, 816
- Kitchener B., Brinks E., Heesen V., Hunter D. A., Zhang H., Rau U., Rupen M. P., Little Things Collaboration, 2015, *Am. Astron. Soc. Meeting Abstr.*, 225, 248.16
- Klein U., Weiland H., Brinks E., 1991, *A&A*, 246, 323
- Krause M., Fierlinger K., Diehl R., Burkert A., Voss R., Ziegler U., 2013, *A&A*, 550, A49
- Lacki B. C., Thompson T. A., Quataert E., 2010, *ApJ*, 717, 1
- Lee J. H., Lee M. G., 2014, *ApJ*, 793, 134
- Leitherer C. et al., 1999, *ApJS*, 123, 3
- Leroy A., Bolatto A., Walter F., Blitz L., 2006, *ApJ*, 643, 825
- Leverenz H., Filipović M. D., Bojičić I. S., Crawford E. J., Collier J. D., Grieve K., Drašković D., Reid W. A., 2016, *Ap&SS*, 361, 108
- Long K. S. et al., 2010, *ApJS*, 187, 495
- Longair M. S., 2011, *High Energy Astrophysics*. Cambridge Univ. Press, Cambridge
- Lozinskaya T. A., Moiseev A. V., 2007, *MNRAS*, 381, L26
- McDonald A. R., Muxlow T. W. B., Pedlar A., Garrett M. A., Wills K. A., Garrington S. T., Diamond P. J., Wilkinson P. N., 2001, *MNRAS*, 322, 100
- Madden S. C. et al., 2013, *PASP*, 125, 600
- Massardi M., Bonaldi A., Negrello M., Ricciardi S., Raccanelli A., de Zotti G., 2010, *MNRAS*, 404, 532
- Massey P., Armandroff T. E., Conti P. S., 1992, *AJ*, 103, 1159
- Miller G. E., Scalo J. M., 1979, *ApJS*, 41, 513
- Nidever D. L. et al., 2013, *ApJ*, 779, L15
- Niklas S., Beck R., 1997, *A&A*, 320, 54
- Nilson P., 1973, *Uppsala General Catalogue of Galaxies*. Acta Universitatis Upsaliensis. Nova Acta Regiae Societatis Scientiarum Upsaliensis - Uppsala Astronomiska Observatoriums Annaler. Astronomiska Observatorium, Uppsala
- Peck L. W., Fenech D. M., 2013, *Astron. Comput.*, 2, 54
- Roychowdhury S., Chengalur J. N., 2012, *MNRAS*, 423, L127
- Sakai S., Madore B. F., Freedman W. L., 1999, *ApJ*, 511, 671
- Salpeter E. E., 1955, *ApJ*, 121, 161
- Sanna N. et al., 2009, *ApJ*, 699, L84
- Shostak G. S., Skillman E. D., 1989, *A&A*, 214, 33
- Silverman J. M., Filippenko A. V., 2008, *ApJ*, 678, L17
- Stockdale C. J., Goss W. M., Cowan J. J., Sramek R. A., 2001, *ApJ*, 559, L139
- Strömgren B., 1939, *ApJ*, 89, 526
- Strong A. W., Moskalenko I. V., Ptuskin V. S., 2007, *Annu. Rev. Nucl. Part. Sci.*, 57, 285
- Vacca W. D., Sheehy C. D., Graham J. R., 2007, *ApJ*, 662, 272
- Vallée J. P., 1995, *Ap&SS*, 234, 1
- Wang Q. D., 1999, *ApJ*, 510, L139
- Wang Q. D., Whitaker K. E., Williams R., 2005, *MNRAS*, 362, 1065
- Weiler K. W., Panagia N., Montes M. J., Sramek R. A., 2002, *ARA&A*, 40, 387
- Wilcots E. M., Miller B. W., 1998, *AJ*, 116, 2363
- Yang H., Skillman E. D., 1993, *AJ*, 106, 1448
- Yun M. S., Reddy N. A., Condon J. J., 2001, *ApJ*, 554, 803

This paper has been typeset from a $\text{\TeX}/\text{\LaTeX}$ file prepared by the author.